Concept Design of a 1.4 MW Drive for Rotor Loss Minimization in a Partially Superconducting Motor

Matthew G Granger, Thomas F Tallerico, Aaron D Anderson, Justin J Scheidler, Pete Kascak, Alex Leary, Ralph Jansen
NASA Glenn Research Center, Cleveland, OH, USA
{matthew.granger, thomas.tallerico, aaron.d.anderson-1, justin.j.scheidler, peter.e.kascak, alex.m.leary, ralph.h.jansen}@nasa.gov

***Abstract*- Partially superconducting machines with cryocooler-cooled rotors are a potential near-term technology that can achieve the motor performance needed by future fixed wing electric aircraft. For this type of machine, minimizing cryogenic heat load is one of the keys for enabling high machine performance. Rotor eddy current loss is often the most difficult cryogenic heat load to mitigate due to current ripple from the motor drive. This paper presents the concept design for a 20 kW/kg, 99.5% efficient motor drive that has sufficiently low current ripple to enable high performance partially superconducting machines by minimizing eddy current loss in the rotor. The motor drive concept design uses a resonant, interleaved, and multilevel topology to achieve these high-performance metrics with little current ripple. Rotor magnetic loss analysis using NASA's 1.4 MW High Efficiency Megawatt Motor (HEMM) is used in the design process to down select the motor drive topology and show that the final design generates less than 5 W of magnetic loss in the rotor.**

I. Introduction

Partially superconducting machines with superconducting rotors are a potential near-term technology capable of achieving the motor performance needed for transport class aircraft utilizing electrified aircraft propulsion (EAP) to have fuel burn and emissions benefits. For these types of machines, minimization of the cryogenic heat load on the rotor and, consequently, either the size of the cryocooler or amount of liquid cryogen required to cool the rotor is key for enabling high overall machine performance. In the case of a cryocooler-cooled rotor, even a relatively small amount of heat can prevent the machine from functioning as intended. Rotor eddy current losses caused by current ripple in the motor drive-supplied waveform is possibly the most difficult source of rotor heat to mitigate in these machines. The most common solution to eliminating rotor eddy currents is to use an eddy current shield. However, these shields come at the cost of increased machine magnetic air gap, increased mass, complicated structures, and in some cases added losses.

This paper presents the concept design of a 1.4 MW motor drive capable of approaching 20 kW/kg specific power and 99.5% efficiency while minimizing current ripple sufficiently to enable less than 5 W of rotor eddy current loss in a cryogenic rotor without the use of an eddy current shield. The target application of this design is to drive NASA's High Efficiency Megawatt Motor (HEMM), a 1.4 MW partially superconducting machine being developed at NASA Glenn Research Center [1] [2] [3] [4] [5] [6] [7] [8]. In [9], the authors showed that the original concept design for the HEMM motor drive could not reduce rotor eddy current losses below the 50 W limit of HEMM's shaft-integrated cryocooler. The new concept design meets this restrictive loss limit through the use of a resonant converter topology and an optimized filtering architecture. This paper describes the design of this motor drive topology to achieve high specific power, efficiency, and low rotor magnetic loss.

Technologies used in this new motor drive topology are described in Section II. Section III then describes the models used to produce the stator current waveforms. Section IV elaborates on the models used to predict the mass and loss of the motor drive's power electronics and output filter. Section V describes the rotor loss model used to evaluate the abilities of different motor drive topologies to achieve low rotor loss. Section VI presents results of studies used to down select the final motor drive design. A conclusion summarizing the key results from the design process and next steps for the motor drive development is given in Section VII.

II. Motor Drive Topology

The motor drive topology studied in this effort is shown in Fig. 1. The inverter is fed by a DC bus, leading into a power electronics section that consists of a multilevel and interleaved auxiliary resonant commutated pole (ARCP) architecture [10]. For visual clarity, the ARCP and multilevel architectures are not shown in the diagram. The power electronics are coupled to the motor through a series of output filters, including both interleaving output inductors and an LC filter.

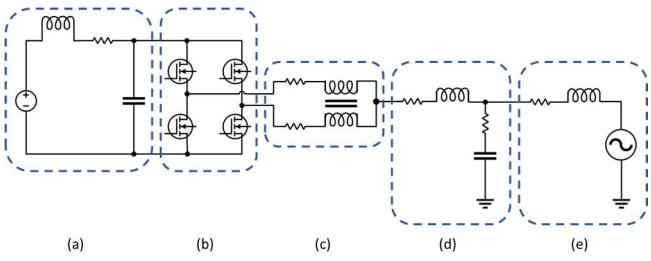

Fig. 1. Electrical topology of motor drive (shown as per-phase, two level, and two interleave). Sections include the (a) DC bus, (b) power electronics, (c) interleaving magnetics, (d) output filter, and (e) motor.

In the inverter design the multilevel architecture is used primarily to increase the voltage rating of the inverter, but it also provides a modest improvement in the harmonic content of the waveform passed to the output filters. The rest of the motor drive topology is included entirely for the sake of reducing superconducting rotor magnetic losses down to acceptable levels by minimizing the harmonic content of the current waveform applied to the stator.

In [9], it was found that the multilevel topology and interleaving alone were not sufficient to reduce rotor losses to acceptable values. Additional output filtering was needed but would not fit into the original design within the mass goal of 20 kW/kg. In the new design, the ARCP is used to increase switching frequency to greater than 100 kHz without dropping motor drive efficiency below 99.5%. With the higher switching frequency, the size of the LC filter needed to smooth the current waveform is reduced to acceptable levels.

The primary advantage of the ARCP topology is the ability to perform zero-current and zero-voltage switching [10]. These features enable the minimization of switching losses at the cost of added resonant circuits. Higher switching frequencies are made possible as a result; however, the higher switching frequency does increase the difficulty of achieving good control and switch timing. Demonstrating functionality and measuring losses for the greater than 100 kHz switching frequencies proposed in this paper is the primary target of risk reduction experiments for this motor drive design.

Interleaving is included as an option in the motor drive design due to uncertainty in the practicality of achieving switching frequencies greater than 100 kHz. Interleaving allows an inverter to operate at a lower switching frequency than what appears at the load, at the cost of increased filter mass due to the interleaving output inductors. Interleaving is not a part of the preliminary motor drive concept design proposed in this paper but may be re-incorporated if the target switching frequency is found to be impractical.

The output LC filter consists of a per-phase series inductance and neutral-connected capacitance. When interfaced with the natural inductance of the motor, the additional inductance and capacitance acts like a current choke and shunt, respectively, to both decrease the amount of high-frequency current in the output circuit, as well as to shunt the remaining high-frequency current away from the stator.

III. Combined Motor Drive-Motor Model

A state space representation of the motor and motor drive was used to simulate stator current waveforms for different possible motor drive designs. The state space model was found to be convenient for this type of analysis, as it facilitates a simple method for deriving steady-state motor waveforms using numerical integration techniques and allows for a simple method of including the motor's inductance matrix as derived from the electromagnetic FEA analysis [9]. The unusual motor drive topology explored in this paper made typical commercial software used for power electronics simulations impractical. Appendix I provides the details of the state space representation of the motor and the motor drive.

These state space models enable the accurate prediction of switching harmonics by incorporating a model of the switching modulation scheme into the system matrix. Accurate modelling of the motor's spatial harmonics is also possible via their inclusion in the back-emf voltage vector. Spatial harmonics are not considered in this study since the harmonic controller described in [9] is assumed to be included in the motor drive's control scheme.

A key result from [9] was that an I^2f^2 metric corresponding to the classical eddy current equation is a better metric than harmonic distortion for estimating rotor losses that would result from a given stator current waveform. To more easily simulate the induced rotor loss caused by different current waveforms without the computational cost of an FEA simulation, a rotor loss estimate was made using

$$P_{rotor} = \sum_{n=1}^{N} \frac{R_{FEA}}{\sqrt{f_n}} \left(I_{f_n}^2 f_n^2\right) \tag{1}$$

where P_{rotor} is the estimated rotor loss, f_n is the frequency of the n^{th} harmonic, R_{FEA} is a constant derived from preliminary FEA simulations of rotor eddy current loss, and I_{f_n} is the current magnitude corresponding to a given frequency in the stator current waveform. R_{FEA} is meant to represent the effective resistance of the rotor to eddy currents. The $\sqrt{f_n}$ term is a correction factor applied to R_{FEA} to account for skin depth changes with harmonic frequency. This less computationally burdensome rotor loss estimate was useful in performing a large parameter sweep for the different motor drive configurations. Results of interest from this large sweep were then simulated in FEA for better accuracy.

IV. Motor Drive Mass and Loss Models

Mass and loss models must be established to evaluate the suitability of different motor drive designs (combinations of switching frequencies and output filter sizes) and their ability both to meet the rotor loss objective as well as the 20 kW/kg specific power and 99.5% efficiency targets. These models are now presented in this section.

Fig. 2 shows curves for the mass of the output filter inductor as a function of inductance and peak current. The geometry of the inductor is a single-turn design, where the core material is made into a toroidal sleeve which fits over the phase cable. The core is made from a custom material produced by researchers at NASA Glenn Research Center [11]. This material exhibits very low loss relative to similar powder core materials. As such the inductor inefficiencies are not a considerable loss driver for the motor drive.

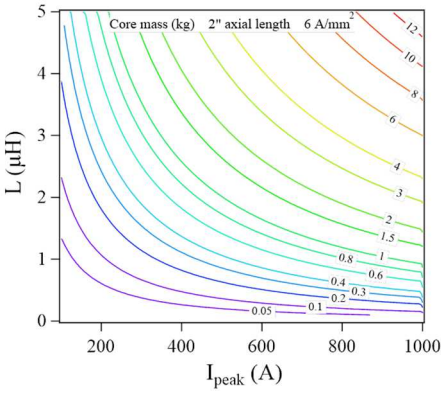

Fig. 2. Core mass for a single-turn inductor made with GRC magnetic material.

Fig. 3 shows mass of the capacitor portion of the motor drive's output filter as a function of capacitance. This plot was produced by an algorithm which calculates the optimal combination of capacitors to place in parallel and series, both to achieve low loss and the appropriate voltage rating, respectively. Enough capacitors are placed in parallel to ensure they are not a major loss contributor for the motor drive. The capacitors are selected from the Wima MKP-4 family [13].

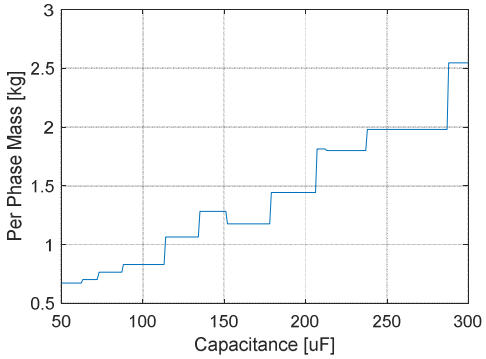

Fig. 3. Mass of the output filter capacitor bank for a single phase, as a function of per-phase capacitance.

In order to achieve the 99.5% efficiency target, the total of all losses in the motor drive must stay below 7 kW. The two major loss drivers in the motor drive are the conduction and switching losses of the MOSFETs. Losses in the output filter also need to be accounted for, although they are expected to contribute considerably less loss than the power electronics.

A plot of conduction losses over a range of switching frequencies for one output filter configuration is shown in Fig. 4. For this plot an assumption is made that the equivalent $R_{ds,on}$ of each MOSFET is 1.23 mΩ at 25°C, which is extrapolated from previous motor drive builds designed by the authors. The low $R_{ds,on}$ is achieved by paralleling and/or interleaving MOSFETs. The conduction loss reduces at higher switching frequencies because of the minimization of high frequency current ripple, which reduces the RMS value of the current through each MOSFET.

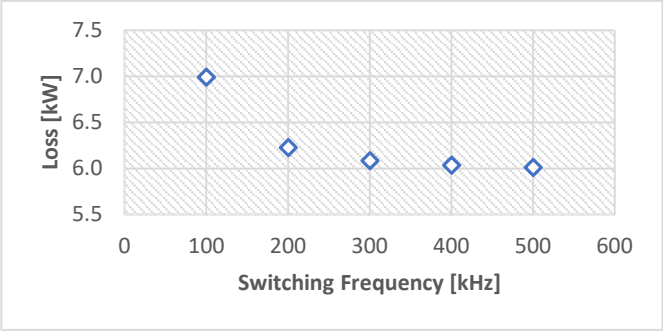

Fig. 4. Conduction loss in the power MOSFETs as a function of switching frequency.

A plot of switching losses for a range of different switching frequencies is shown in Fig. 5. For this plot an assumption is made as to the switching and conduction performance of the MOSFETs, which was extrapolated from previous motor drive builds designed by the authors. Soft switching losses are shown for the ARCP topology along with what losses would be with a hard switching scheme. Conduction losses in the resonant circuitry occur at every commutation, and so are considered switching loss, even though the ARCP exhibits no classical hard switching loss. The significant benefit of the ARCP topology is shown.

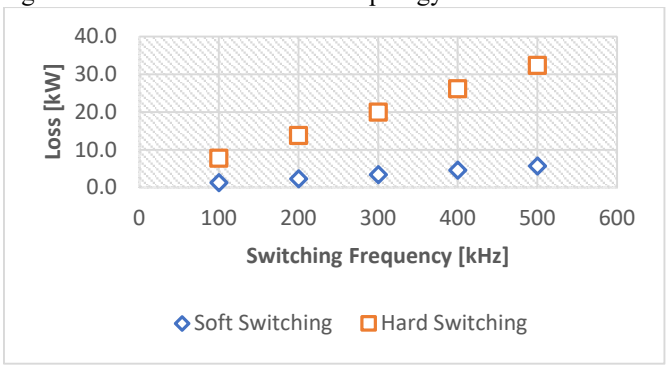

Fig. 5. Switching losses in the power MOSFETs as a function of switching frequency. Both hard and soft switching losses are shown.

As will be shown in section VI, the optimum switching frequency is found to be 200 kHz. Per the previous figures, total power electronics losses at 200 kHz sum to 8.6 kW. This results in an efficiency slightly below the desired level. Further optimizations can be made to meet the efficiency goal, including further refinement of the MOSFET selection, or increasing the number of switching devices used in parallel.

V. Rotor Loss Model

A time stepping FEA of NASA's HEMM motor was used first to tune the analytical model for rotor loss used in the motor drive optimization (Equation 1), and then as a final analysis of rotor loss for selected designs. Both mesh and time step refinement studies were carried out to develop the simulation for evaluation of the motor drive waveforms. The mesh used on a single rotor tooth is depicted in Fig. 6. A boundary layer mesh with 20 layers, a first element thickness of 50 μm, and a growth rate of 1.02 is used at the outer radial edge of both the rotor core teeth and the titanium coil support cups to capture the eddy currents in the rotor.

The FEA simulation was carried out in 3 steps. First a static ramping of rotor and stator current was carried out to the target nominal currents for HEMM. Then an initial low convergence time stepping simulation was carried out with 50 ns time steps for 20 μs to create a good initial condition for the final simulation step. The final simulation step was carried out with tight convergence and a 5 ns time step for 5 μs. Eddy current losses were evaluated at both the rotor core tooth and in the titanium coil support structure. Example flux density, rotor eddy current, and loss plots for the simulation are depicted in Fig. 7.

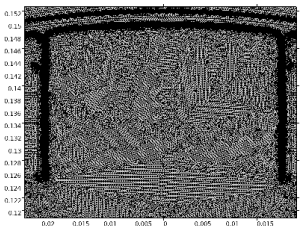

Fig. *6* Mesh on a single rotor tooth in the time stepping FEA simulation.

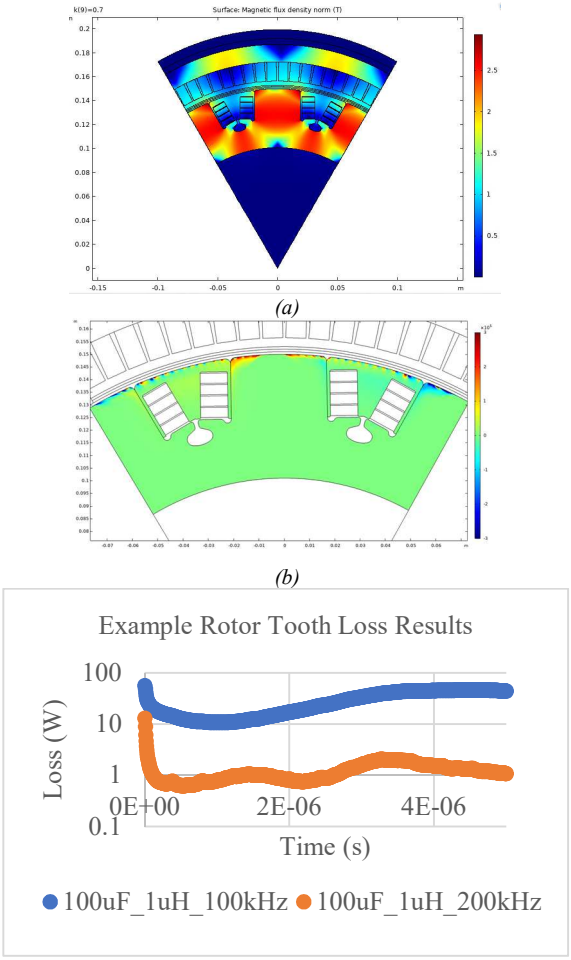

Fig. *7*. Results of rotor loss FEA analysis, (a) motor cross-sectional view plot of magnetic flux density, (b) FEA simulated rotor eddy currents for a high-performance design, and (c) example rotor loss curves over the simulation.

VI. Model Results and Topology Selection

For preliminary design of the motor drive, parametric sweeps of switching frequency and filter size were carried out using the state space model. Fig. 8 summarizes all designs that were estimated to be able to produce less than 10 W of rotor loss based on Equation 1 with a switching frequency less than 300 kHz and a filter mass less than 20 kg. From the results, eight waveforms were selected and simulated explicitly using the rotor loss FEA simulation. The selected designs and their resulting rotor loss estimates are summarized in Table 1. The plot in Fig. 9 shows rotor loss and filter mass for the FEA analyzed data. The rotor loss estimates generated by Equation 1 generally over estimated rotor loss for the selected designs relative to the FEA based prediction, but largely predicted the same trends and were in reasonable agreement in total magnitude. Further development of Equation 1 could improve accuracy, but present results show the low rotor loss motor drive design methodology used here to be sufficient for preliminary design.

For the preliminary concept design of the motor drive, the 200 kHz, 80 µF, 1.5 µH design from Table 1 was selected. The 200 kHz was selected over 250 kHz to reduce control and switch timing difficulties and uncertainties. The 80 µF and 1.5 µH filter was selected since it was the lowest rotor loss design that has an estimated filter mass less than 20 kg. Although the lower mass designs at 200 kHz are also predicted to have less than 5 W of rotor loss, simulation uncertainty necessitates that margin on the 5 W rotor eddy current loss target be maximized at this stage in the motor drive design.

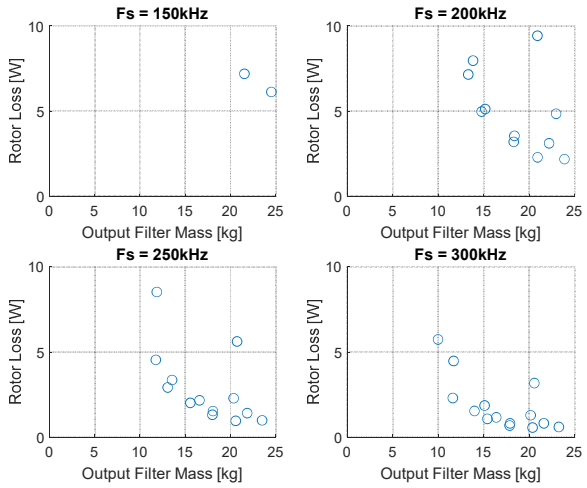

Fig. 8. Rotor loss and output filter mass for several different motor drive switching frequencies. Rotor loss simulated via Equation 1.

TABLE 1
OUTPUT FILTER MASS AND ROTOR LOSS RESULTS. ROTOR LOSS SIMULATED IN FEA.

Motor Drive Switching Frequency [kHz]	Output Filter Capacitance [µF]	Output Filter Inductance [µH]	Output Filter Mass [kg]	Rotor Loss [W]
150	100	1.5	21.5	3.76
150	150	1.2	24.5	3.33
200	80	1	13.3	4.14
200	80	1.2	14.8	3.55
200	80	1.5	18.3	3.33
200	100	1.5	20.9	2.85
250	80	0.8	11.7	3.19
250	80	1.5	18.0	2.57

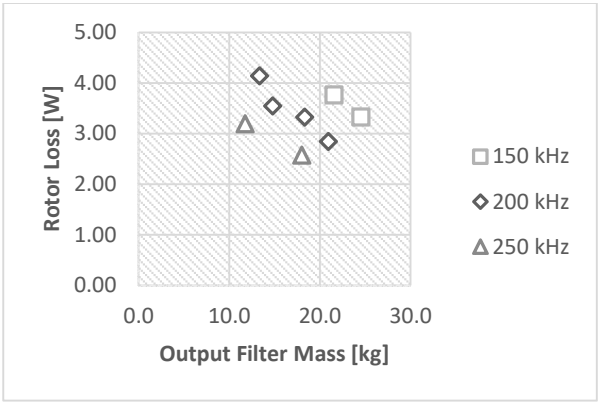

Fig. 9. Pareto fronts of rotor loss and output filter mass for the FEA analyzed datasets.

VII. Conclusion

In this paper, the concept design for a motor drive capable of minimizing stator current ripple causing superconducting motor rotor eddy current loss without the use of an eddy current shield was presented. An analysis methodology for developing low rotor loss motor drive topologies was presented and used to develop the design. The selected concept design is projected to be able to minimize rotor eddy current loss in NASA's partially superconducting HEMM to less than 5 W while simultaneously achieving a motor drive specific power greater than 20 kW/kg and an efficiency approaching 99.5%. Near term future work in this area will focus on demonstrating high frequency control of the ARCP topology, gaining accurate loss measurements for the switches with non-ideal control, and refining and building the final version of the motor drive for use in the testing of the HEMM.

Acknowledgment

This work was supported by the Power and Propulsion Subproject within the Advanced Air Transport Technology Project of NASA's Aeronautics Research Mission Directorate. Additional support was provided by the Convergent Aeronautics Solutions Project of NASA's Aeronautics Research Mission Directorate.

Appendix I: Electrical State Space System

The full set of state space equations which describe the motor drive and motor system are shown in Fig. 10. These equations describe the system shown schematically in Fig. 1. The individual matrices and vectors are described in detail in Table 2-Table 5.

$$\begin{cases} L_b\dot{I_b} = -R_bI_b - \overrightarrow{e_1^T}V_b + V_{dc} \\ C_b\dot{V_b} = -(n-1)C_cS_w^TI_i + (n-1)C_c\overrightarrow{e_1}I_b \\ [L_i + C_vL_fC_i]\dot{I_i} = -[R_i + C_vR_LC_i + C_vR_cC_i]I_i - C_vV_c + C_vR_cI_p + S_wV_b - V_n \\ C_f\dot{V_c} = C_iI_i - I_p \\ L_m\dot{I_p} = -[R_c + R_m]I_p + R_cC_iI_i + V_c - V_{bemf} \end{cases}$$

Fig. 10. Set of electrical state space equations describing multilevel, interleaved, resonant, multiphase inverter. The vector $\overrightarrow{e_1}$ refers to the unit vector with 1 in the first entry.

TABLE 2
DESCRIPTIONS OF DIMENSIONS

Parameter	Dimension
Number of phases	p
Number of interleaves per phase	m
Number of inverter levels	n

TABLE 3
DESCRIPTIONS OF STATE VARIABLES

Variable	Name	Description	Dimensions
I_b	DC Bus Current	Current travelling from the DC bus into the inverter.	Scalar
V_b	DC Link Capacitor Voltages	Voltages across each of the stacked DC link capacitors with respect to DC bus return. The first entry is the capacitor closest to DC bus positive, and the rest are in order going down to the capacitor nearest DC bus return.	$(n-1)$ x 1
I_i	Interleave Currents	The currents through each leg of the interleave inductors.	(pm) x 1
I_p	Stator Currents	The currents through each of the phases of the motor.	p x 1
V_c	Output Filter Capacitor Voltages	The voltage across each of the output filter capacitors with respect to V_n.	p x 1

TABLE 4
DESCRIPTIONS OF ELECTRICAL COMPONENT VARIABLES

Variable	Name	Description	Dimensions
L_b	Bus Inductance	Series inductance of the DC bus.	Scalar
R_b	Bus Resistance	Series resistance of the DC bus.	Scalar
C_b	Bus Capacitors	Diagonal matrix describing values of the stacked DC link capacitors.	$(n-1)$ x $(n-1)$
L_i	Interleave Filter Inductance	Inductance matrices describing the interleave inductors.	(pm) x (pm)
R_i	Interleave Filter Resistance	Resistance matrices describing the interleave inductors.	(pm) x (pm)
L_f	Output Filter Inductance	Matrix describing values of the series inductor used for output filtering.	p x p
R_L	Output Filter Inductor Resistance	Matrix describing values of the series resistance used for output filtering.	p x p
C_f	Output Filter Capacitance	Matrix describing values of the shunt capacitors used for output filtering.	p x p
R_c	Output Filter Capacitor Resistance	Matrix describing values of the shunt resistors used for output filtering.	p x p
L_m	Motor Inductance	Inductance matrix describing the motor.	p x p
R_m	Motor Resistance	Resistance matrix describing the motor.	p x p
V_{dc}	DC Bus Voltage	Value of the DC bus supply voltage.	Scalar
V_n	Motor Neutral Voltage	Voltage of the motor's neutral, with respect to DC bus return. All entries of the vector are identical.	p x 1
V_{bemf}	Motor Back-emf Voltage	The back-emf voltages of each phase with respect to V_n.	p x 1

TABLE 5
DESCRIPTIONS OF HELPER MATRICES AND VECTORS

Variable	Name	Description/Definition*	Dimensions
C_v	Transformation Matrix from Per Phase to Per Interleave	$\mathbf{I}_{pxp} \otimes \mathbf{J}_{mx1}$	pm x p
C_i	Transformation Matrix from Per Interleave to Per Phase	$\mathbf{I}_{pxp} \otimes \mathbf{J}_{1xm}$	p x pm
S_w	Interleave Leg Voltage State Matrix	Time varying matrix which describes how switches connect the interleave leg outputs to the DC link capacitors. No more than one entry in a row is set to 1, and the rest are set to 0. If the column with the 1 entry is column i, then the voltage on the output of the leg is $V_{b,i}$. If a row is all 0's, the output voltage is 0 V.	pm x $(n-1)$
C_c	DC Link Capacitor Connection Matrix	$C_{b,i,j} = n - j - \max(0, i-j)$	$(n-1)$ x $(n-1)$

*I refers to the identity matrix, J refers to a matrix of all ones, and $\otimes$ is the Kronecker product.
**Rows and columns of dimension p are ordered like phase A, phase B, etc. Rows and columns of dimension pm are ordered like phase A interleave 1, phase A interleave 2, …, phase A interleave m, phase B interleave 1, etc.

References

[1] R. H. Jansen, Y. De Jesus-Arce, P. Kascak, R. Dyson, A. Woodworth, J. J. Sheidler, R. Edwards, E. Stalcup, J. Whilhite, K. Duffy, P. Passe and S. McCormick, "High Efficiency Megawatt Motor Conceptual Design," in *AIAA Propulsion and Energy Forum*, Cincinnati, 2018.

[2] R. H. Jansen, P. Kascak, R. Dyson, A. Woodworth, J. Scheidler, A. D. Smith, T. Tallerico, Y. De Jesus-Arce, D. Avanesian, K. Duffy, P. Passe and G. Szpak, "High Efficiency Megawatt Motor Preliminary Design," in *AIAA/IEEE Electric Aircraft Technologies Synmposium*, Indianapolis, 2019.

[3] R. H. Jansen, J. Scheidler, T. Tallerico, P. Kascak, A. Woodworth, A. Smith, R. Dyson, W. Sixel, J. Thompson, E. Stalcup, Y. De Jesus-Acre, D. Avanesian, K. Duffy, P. Passe and G. Szpak, "High Efficiency Megawatt Motor Risk Reduction Activities," in *Electrified Aircraft Technologies Symposium*, New Orleans, 2020.

[4] G. Sapak, A. Smith, J. T. Thompson, A. Woodworth and R. Jansen, "High Efficiency Megawatt Motor Thermal Stator Preliminary Design," in *AIAA/IEEE Electrified Aircraft Technologies Symposium*, New Orleans, 2020.

[5] J. J. Scheidler and T. F. Tallerico, "Design, Fabrication, and Critical Current Testing of No-Insulation Superconducting Rotor Coils for NASA's 1.4 MW High-Efficiency Megawatt Motor," in *AIAA/IEEE Electric Aircraft Technologies Symposium*, Cincinnati, 2018.

[6] J. J. Sheidler, T. F. Tallerico, W. A. Miller and W. Torres, "Progress Toward the Critical Design of the Superconducting Rotor for NASA's 1.3 MW High-Efficiency Electric Machine," in *AIAA/IEEE Electric Aircraft Technologies Symposium*, Indianapolis, 2019.

[7] A. A. Woodworth, A. Smith, W. Sixel, R. Edwards, R. Jansen, S. McCormick, M. Robbie, G. Szpak, P. Naghipour and E.-S. Shin, "Thermal Analysis of Potted Litz Wire for High-Power-Density Aerospace Electric Machines," in *AIAA Propulsion and Energy Forum*, Indianapolis, 2019.

[8] T. Tallerico, J. Scheidler, D. Lee and K. Haran, "Electromagnetic Redesign of NASA's High Efficiency Megawatt Motor," in *AIAA/IEEE Electric Aircraft Technologies Symposium*, Virtual, 2020.

[9] M. G. Granger, A. Aaron, J. M. Maroli, T. Tallerico and J. J. Scheidler, "Combined Analysis of NASA's High Efficiency Megawatt Motor and Its Converter," in *AIAA Propulsion and Energy Forum*, Virtual, 2021.

[10] R. De Doncker and J. Lyons, "The auxiliary resonant commutated pole converter," in *IEEE Industry Applications Society Annual Meeting*, Seattle, WA, 1990.

[11] A. Leary, V. Keylin, R. Noebe, R. Bowman, G. Feichter, K. Byerly, P. Ohodnicki and M. McHenry, "Core Losses in Co-rich Inductors with Tunable Permeability," in *TMS Annual Meeting and Exhibition*, 2020.

[12] V. Venkatachalam, C. Sullivan, T. Abdallah and H. Tacca, "Accurate Predicition of Ferritie Core Loss with Non-Sinusoidal Waveforms Using only Steinmets Parameters," in *Computers in Power Electronics* , Mayaguez, 2002.

[13] Wima, "DC-LINK MKP 4," [Online]. Available: https://www.wima.de/en/our-product-range/dc-link-capacitors/dcl-mkp-4/.